Three-dimensional Topological Insulator Tunnel Diodes

Stephen P. Fluckey[1], Sabyasachi Tiwari[2,3,4], Christopher L. Hinkle[5], and William G. Vandenberghe[2]
[1] *Department of Physics, The University of Texas at Dallas, 800 W Campbell Rd., Richardson, Texas 75080, USA.*
[2] *Department of Materials Science and Engineering, The University of Texas at Dallas, 800 W Campbell Rd., Richardson, Texas 75080, USA.*
[3] *Department of Materials Engineering, KU Leuven, Kasteelpark Arenberg 44, 3001 Leuven, Belgium.*
[4] *Imec, Kapeldreef 75, 3001 Heverlee, Belgium.*
[5] *Department of Electrical Engineering, The University of Notre Dame, Notre Dame, Indiana 46556, USA and*
Email: william.vandenberghe@utdallas.edu

Topological insulators open many avenues for designing future electronic devices. Using the Bardeen transfer Hamiltonian method, we calculate the current density of electron tunneling between two slabs of Bi_2Se_3. 3D TI tunnel diode current-voltage characteristics are calculated for different doping concentrations, tunnel barrier height and thickness, and 3D TI bandgap. The difference in the Fermi levels of the slabs determines the peak and trough voltages. The tunnel barrier width and height affect the magnitude of the current without affecting the shape of the current-voltage characteristics. The bandgap of the 3D TI determines the magnitude of the tunnel current, albeit at a lesser rate than the tunnel barrier potential, thus the device characteristics are robust under changing TI material. The high peak-to-trough ratio of 3D TI tunnel diodes, the controllabilty of the trough current location, and the simple construction provide advantages over other NDR devices.

I. INTRODUCTION

Recent advances in the field of topological insulators [1] have opened a plethora of opportunities for their use in both charge-based [2, 3] and spin-based devices [4, 5]. TIs have been proposed for many exotic applications including quantum computation [6], lasing [7], and skyrmion-based devices [8]. Some recent proposed applications are electrochemical energy storage [9] and mode-locked lasers [10]. Electric-field control of the surface state spin-polarization opens a plethora of opportunities in building spin-based devices using Bi_2Se_3 including, superconductivity [11], photodetectors [12], and tetrahertz frequency generation [13].

Topological Insulators are a class of material with spin-momentum locked surface or edge states. Topological insulators are classified as either two-dimensional (2D) or three-dimensional (3D). A 2D TI has an insulating 2D bulk and a conducting edge, while a 3D TI has an insulating bulk and conducting surface. 3D TIs are arguably more promising for short-term device applications than 2D TIs because well-known materials like Bi_2Se_3 are 3D TIs while 2D TIs rely on more exotic materials [2] like stanene [14, 15] and bismuthene [16]. Surface states of 3D TIs have the interesting property that they have a Dirac dispersion and that their spin and momentum is locked [3]. Previous device proposals have exploited the spin-momentum locking to convert charge to spin [17]. Here we will take a different approach and exploit the spin-momemtum locking of 3D TI surface states to block tunneling current and realize an NDR device[18].

Negative-differential resistance (NDR) devices are a class of electronic devices with non-linear current-voltage characteristics. Due to their unusual response to applied voltage, they are used in many applications such as fast memories, high-frequency devices, frequency-multipliers, and fast switching devices [19].

Unfortunately, present day NDR devices are less controllable in terms of the location of the minima and come with a fixed peak-to-trough ratio [20]. Although some new devices based on nanoscale molecular junctions [21] , and graphene nanoribbons [22] have been proposed to remedy the relatively little control possessed in many current the NDR devices, the diffculty in fabricating such devices presents a roadblock for their practical application [23, 24]. The difficulty in fabricating 2D NDR devices has been noted in both graphene nanoribbons [23], and graphene quantum dots [25]. The development of a 3D TI NDR device could potentially solve many of these issues.

In this work, we investigate a two-terminal NDR device using two 3D TI slabs separated by a tunnel barrier. First, we model the electronic structure of 3D TIs and present the theoretical formulation for calculating the tunneling current. We then show the NDR characteristics of the proposed device, and discuss various control parameters which can be tuned to control the characteristics of the device. We show that the presented device provides a very high peak to trough ratio along with an efficient control over the position of the trough. Finally we discuss the results and their implications and conclude.

II. DEVICE STRUCTURE AND THEORETICAL MODEL

II.1. Device Structure

Figure 1(a) shows the schematic of the Bi_2Se_3 device under investigation. The device comprises of two TIs

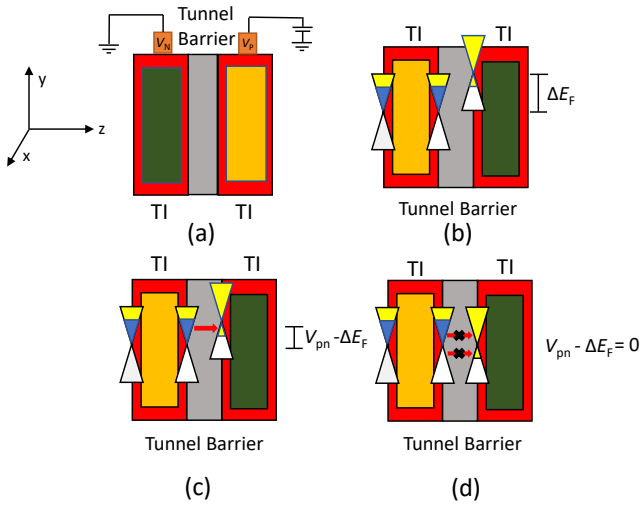

FIG. 1: (a) Device schematic for our proposed TI tunnel diode NDR device. The top slab is p-doped and connected to bias while the bottom slab is n-doped and grounded. The p-doped and n-doped slabs have thickness $t_{\rm p} = t_{\rm n} = 10$ nm. The tunnel barrier's default thickness is $t = 1.0$ nm. (b) Relative position of TI slab Dirac cones due to $\Delta E_{\rm F}$ at zero bias. (c) Relative position of the TI slab Dirac cones at bias $V_{\rm pn}$ less than $\Delta E_{\rm F}$. (d) Relative position of the TI slab Dirac cones at bias $V_{\rm pn}$ equal to $\Delta E_{\rm F}$.

separated by a tunnel barrier. The two slabs of Bi_2Se_3 are assumed to have a different Fermi level as determined by their doping [26, 27]. The spin-polarized conducting surface states are illustrated by the surfaces of the two slabs. The top and bottom slabs are given different colors in our schematic to reference the difference in the Fermi levels ($\Delta E_{\rm F}$) of the two slabs shown in Fig. 1(b). The top slab, which is p-doped, is connected to a voltage source to set the bias $V_{\rm pn}$ and the bottom slab, which is n-doped, is grounded. The total device thickness in our simulations is taken to be 21 nm with a slab size of 10 nm for the top and the bottom slabs, and a tunnel barrier thickness of 1 nm. The thickness in the transverse directions are considered to be infinite.

II.2. Device Operation

Figure 1 (b-d) illustrate the position of the Dirac cones of the surface states of both the slabs at different applied bias ($V_{\rm pn}$). Fig. 1(b), shows the Dirac cones when no bias is applied ($V_{\rm pn}$=0). In Fig. 1(c), the Dirac cone of the top slab shifts down due to an applied bias $0 < V_{\rm pn} < \Delta E_{\rm F}$. With an applied bias, a finite tunneling current flows between the slabs as indicated by the red arrow. The tunneling occurs between the surface states of the n-doped and p-doped slabs. Fig. 1(d), shows the case when the applied bias equals the Fermi level difference ($V_{\rm pn} = \Delta E_{\rm F}$), the Dirac cones of the surface states now match perfectly. However, the surface states have opposite spin-momentum locking which will make the tunneling current vanish. Momentum and energy can be conserved but spin can not because of the opposite spin-polarization of both surface states.

II.3. Electronic Structure of Slabs

We model the TIs and the tunnel barriers using a $\mathbf{k}\cdot\mathbf{p}$ Hamiltonian to describe the TI device performance. We use the Bi_2Se_3 Hamiltonian from Ref. [28],

$$\mathcal{H}(\mathbf{k}) = \epsilon_0(\mathbf{k})\mathcal{I} + \begin{pmatrix} \mathcal{M}(\mathbf{k}) & A_1 k_z & 0 & A_2 k_- \\ A_1 k_z & -\mathcal{M}(\mathbf{k}) & A_2 k_- & 0 \\ 0 & A_2 k_+ & \mathcal{M}(\mathbf{k}) & -A_1 k_z \\ A_2 k_+ & 0 & -A_1 k_z & -\mathcal{M}(\mathbf{k}) \end{pmatrix} \quad (1)$$

where $k_\pm = k_x \pm i k_y$, $\epsilon_0(\mathbf{k}) = C + D_1 k_z^2 + D_2(k_x^2 + k_y^2)$, $\mathcal{I}$ is a 4×4 identity matrix, and $\mathcal{M}(\mathbf{k}) = M - B_1 k_z^2 - B_2(k_x^2 + k_y^2)$. The directions x, y are defined as being in-plane with the TI surface and have rotational symmetry in the $\mathbf{k}\cdot\mathbf{p}$ Hamiltonian. The z direction is defined as being the out-of-plane direction. k_x, k_y, and k_z are the wave-vector components in the x, y, and z directions. The parameters B_1, B_2, C, D_1, D_2, and M are presented in Table I and were previously determined for Bi_2Se_3 in Ref. [28] by fitting to the bulk Bi_2Se_3 band structure obtained from *ab initio* DFT calculations. These parameters give us the slab Hamiltonian $\mathcal{H}_{TI,p}$ and $\mathcal{H}_{TI,n}$.

We use vacuum as the interface tunnel barrier as Bi_2Se_3 is a Van der Waals material. To model the Hamiltonian of this tunnel barrier, $\mathcal{H}_{\rm T}$, we set parameters to that of a free electron with a 1 eV on-site potential [3] to mimic a tunnel barrier with a 1 eV barrier. The parameters D_1=D_2=3.8 eV·Å^2 $= \hbar^2/(2m_e)$, where $\hbar$ is the reduced Planck constant, are chosen to give the electron the free electron mass in the tunnel barrier.

To apply a Fermi shift of $\Delta E_{\rm F}$, we add a term $\Delta E_{\rm F}$ to the diagonal elements of the Hamiltonian in Eq. (1). We apply a bias by subtracting $V_{\rm pn}$ from $\Delta E_{\rm F}$ and treating this as the new effective Fermi shift for $H_{\rm TI,p}$.

In Fig. 2, we show the band structure of a TI slab. The left side of Fig. 2 represents the bottom, n-doped, slab without any Fermi level shift, while the right side represents the top, p-doped, slab with a Fermi level shift of 0.10 eV at zero applied bias. The p-doped and n-doped Fermi levels are represented by dotted lines. It can be observed that doping has created a difference between the p-doped and n-doped Fermi levels. To compute the wave functions in the out-of-plane direction, z, we convert k_z to $i\frac{d}{dz}$, and discretize the Hamiltonian in Eq. (1) using finite differences as detailed in Sec. VI.1. The spin-polarized surface states of the top and bottom slab have different energies because of the 0.1 eV relative Fermi level difference.

	Bi_2Se_3	Tunnel barrier
M	0.28 eV	0 eV
A_1	2.2 eV· Å	0 eV· Å
A_2	4.1 eV· Å	0 eV· Å
B_1	10 eV· Å^2	0 eV· Å^2
B_2	56.6 eV·Å^2	0 eV·Å^2
C	-0.0068 eV	1 eV
D_1	1.3 eV·Å^2	3.8 eV·Å^2
D_2	19.6 eV·Å^2	3.8 eV·Å^2

TABLE I: $\mathbf{k}\cdot\mathbf{p}$ parameters for Bi_2Se_3 [28] and the tunnel barrier. These values are used unless noted otherwise.

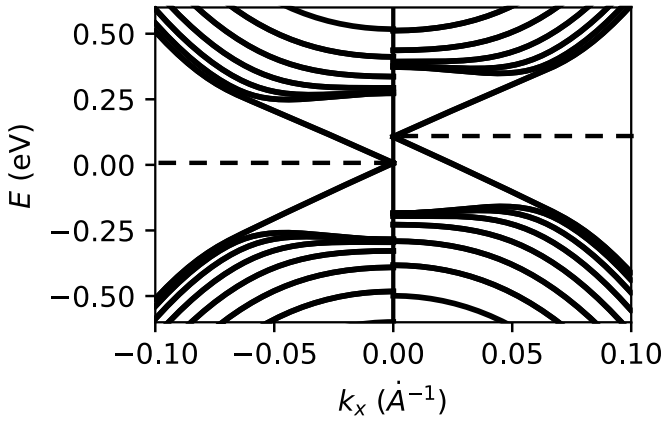

FIG. 2: Band structure of a TI slab of 10 nm thickness plotted in the x and y directions transverse to tunneling. The left hand side has no Fermi level shift, while the right hand side has a Fermi level shift, ΔE_F, of 0.1 eV. The dotted lines represent the effective Fermi level of the p-doped and n-doped slabs with this Fermi level shift.

VI.II rewrite:

To calculate the bandstructure of a TI slab we start with the kdotp Hamiltonian from equation (1). However, since we are calculating the transmission through a slab with a connected dielectric, we must modify this Hamiltonian. To do this, we augment the total Hamiltonian as shown in eq... for the p-doped slab and eq... for the n-doped slab. These Hamiltonians contains the slab and dielectric Hamiltonians and connection terms in the off-diagonal terms. To get a slab bandstructure as opposed to a bulk, we discretize in the out-of-plane direction by replacing k_z with $-i\partial/\partial z$. To find the bandstuctures numerically we use the finite difference method.

The finite difference method replaces ... by ... and ... by ... where ... is the step size. In our case, we took a step size of 1 A. This leads to 96 in the TI slab and 114 steps in the dielectric. So solve the Hamiltonian numerically, for both the slab and dielectric Hamiltonians we take a kronecker product of the matrix and an identity matrix of dimensions of 96X96 for the slab and 114X114 for the dielectric. These matrices once again form the diagonal blocks of our discretized matrix. In order for our final system Hamiltonian to still be a square matrix, the dimensions of the connection terms are set such that the final matrix has

II.4. Tunneling Current

We use the Bardeen transfer Hamiltonian method [29] to calculate the tunneling current between the TI slabs. The Bardeen transfer Hamiltonian follows from time-dependent perturbation theory [30], which treats the Hamiltonian of the intervening barrier as a perturbation.

We sum over the intersecting pairs of bands μ_j and η_j with band index j. By integrating over the 1D first Brillouin zone and by requiring energy conservation, the current is determined by the intersection of $E_{p\mu}(k)$ and $E_{n\eta}(k)$. Summing over pairs of intersecting bands with index μ and η leads to the probability of transition between the p-doped and n-doped slabs

$$P = \frac{2\pi}{\hbar}\sum_j \int\int \frac{dk_x}{2\pi}\frac{dk_y}{2\pi}|M_j|^2\delta(E_{n\mu_j}(k) - E_{p\eta_j}(k)) \tag{2}$$

where $|M_j| = |\Psi_{n\mu_j}(\kappa_j)\frac{d\Psi_{p\eta_j}(\kappa_j)}{dz} - \Psi_{p\eta_j}(\kappa_j)\frac{d\Psi_{n\nu_j}(\kappa_j)}{dz}|$ is the transition matrix element corresponding to the transition between the wave functions of bands $E_{p\mu}(k)$ and $E_{n\eta}(k)$ for $k = \sqrt{k_x^2 + k_y^2}$.

Since our Hamiltonian exhibits in-plane rotational symmetry, we convert to a polar coordinate system where $k_x = k\cos(\theta)$ and $k_y = k\sin(\theta)$. We use $k^2 = k_x^2 + k_y^2$ and $dk_x dk_y = kdkd\theta$ to arrive at:

$$P = \frac{1}{\hbar}\sum_j \int kdk|M_j|^2\delta(E_{n\mu_j} - E_{p\eta_j}) \tag{3}$$

to integrate over k we change $\delta(E_{p\mu} - E_{n\eta})$ to a function of k using $\delta(E_{n\mu} - E_{p\eta}) = \delta(k_{n\mu} - k_{p\eta})\left|\frac{\mathrm{d}((\mathrm{E_{p\mu}(k)}) - (\mathrm{E_{n\eta}(k)}))}{\mathrm{d}k}\right|^{-1}$.

Evaluating the integral in Eq. (4):

$$P = \frac{1}{\hbar}\sum_j \kappa_j \left|\frac{\mathrm{d}(\mathrm{E_{p\mu_j}(k)} - \mathrm{E_{n\eta_j}(k)})}{\mathrm{d}k}\right|^{-1}_{k=\kappa_j}|M_j|^2 \tag{4}$$

where κ_j is the k value at the intersection point.

To model the current density resulting from this transmission probability, we multiply by the electron charge q and the difference in the Fermi-Dirac distribution functions $f(E_n) - f(E_p)$:

$$J = \frac{q}{\hbar}\sum_j \kappa_j|M_j|^2\left|\frac{\mathrm{d}(\mathrm{E_{p\mu_j}(k)} - \mathrm{E_{n\eta_j}(k)})}{\mathrm{d}k}\right|^{-1}_{k=\kappa_j} (f(E_{p\mu_j}(\kappa_j) - V_{\mathrm{pn}}) - f(E_{n\eta_j}(\kappa_j))) \tag{5}$$

where V_p and V_n are the n-doped and p-doped voltages, respectively, whose difference is V_{pn}.

We use 4500 k-points to calculate the band structure of the slabs. We take a step size of $\Delta z = 1$ $\dot{A}$. We model the performance of our TI device at room temperature. We consider the eight energy bands closest to the Fermi level in the calculation of the current as these bands give the largest contribution to tunneling current. Because of the bands considered, we only encounter, at most, one intersection between any two bands. In the case of multiple intersections a summation over a different κ would be required. Calculating additional bands gives additional possibilities for tunneling and thus increases the current, but this increase does not change the shape of the J-V curves we will see in the next section and is negligible for additional considered bands beyond eight. A more detailed examination of the change in the current which results from calculating additional bands can be seen in VI.2.

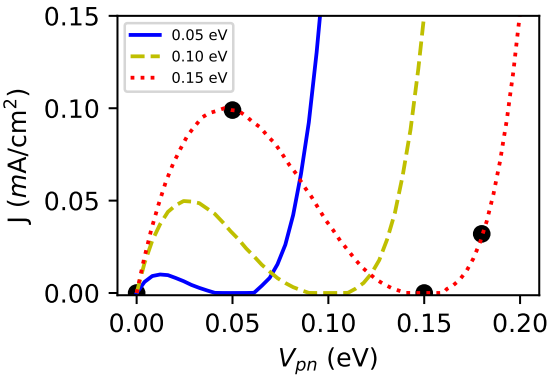

FIG. 3: Current density of our proposed TI NDR device with Fermi level shift $\Delta E_{\rm F} = 0.05$ eV, $\Delta E_{\rm F} = 0.10$ eV, and $\Delta E_{\rm F} = 0.15$ eV. The black dots represent bias points for which the band structure and wave functions are calculated in Fig. 4

III. RESULTS AND DISCUSSION

III.1. Current Density

Figure 3 shows the calculated current density J as a function of $V_{\rm pn}$with Fermi level shifts ($\Delta E_{\rm F}$) of 0.05 eV, 0.10 eV, and 0.15 eV on the top slab. We observe that the current initially increases linearly with the applied $V_{\rm pn}$. However, at $V_{\rm pn} \approx \Delta E_{\rm F}/3$, the current peaks and starts decreasing and goes to almost zero at $V_{\rm pn}$=$\Delta E_{\rm F}$, resulting in NDR behavior. Interestingly, we find that unlike conventional NDR devices whose trough current remains finite [20], because of the very small trough current, the peak to trough ratio is very high. For bias $V_{\rm pn}$>$\Delta E_{\rm F}$, the current starts to increase again. We also observe from Fig. 3 that the maximum current and the trough bias are both determined by the difference in the Fermi level between the TI slabs.

To further analyze the device characteristics, we show the band structure and the wave function of the top and the bottom TI slab at $V_{\rm pn}$= 0 eV, 0.05 eV, 0.15 eV, and 0.18 eV in Fig. 4(a), (b), (c), and (d), respectively. We choose a $\Delta E_{\rm F} = 0.15\ eV$, which corresponds to the red dotted curve in Fig. 3. The wave functions on the right are calculated at an intersection point between the two bands for each bias point.

Figure 4(a) shows the band structure and the wave functions at $V_{\rm pn}$= 0 eV. Although there are states available for tunneling, the zero bias causes the tunneling current to remain zero (first black dot in Fig. 3). Figure 4(b) shows the band structure and the wave functions at a bias $V_{\rm pn}$= 0.05 eV which corresponds to the second black dot in Fig. 3. We now have two, same-spin surface states intersecting shown by the red dots in Fig. 3(c) (band structure). We see that the wave functions of the same

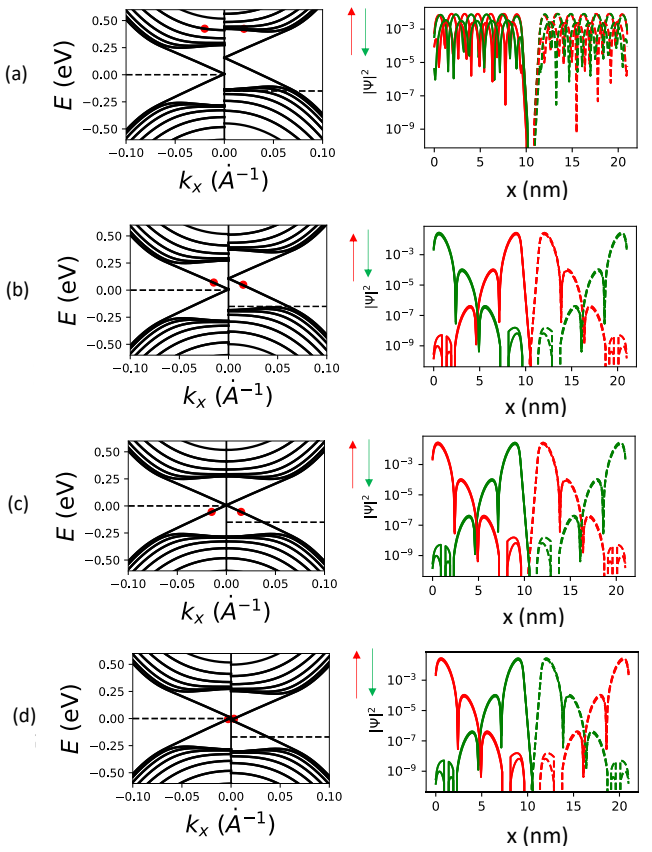

FIG. 4: Band structure of Bi_2Se_3 for different applied biases $V_{\rm pn}$. The red dot indicates a chosen intersection for consideration and the wave functions calculated at that intersection point are plotted to the right. (a) $V_{\rm pn}$= 0 eV we have two bulk state intersections and no current. (b) $V_{\rm pn}$= 0.05 eV we have two same-spin surface state intersections and finite tunneling current. (c) $V_{\rm pn}$= 0.15 eV we have two opposite-spin surface state intersections and nearly zero tunneling current. (d) $V_{\rm pn}$= 0.18 eV we have two same-spin surface states intersections and finite tunneling current.

spin overlap results in a finite tunneling current. We see in Fig. 3 that the tunneling current increases from zero bias up until a bias which is approximately one third of the Fermi level difference between the two slabs.

Figure 4(c) shows the band structure and the wave functions at a bias $V_{\rm pn}$= 0.15 eV. This corresponds to the third black dot in Fig. 3. Now, we have two opposite-spin surface states intersecting. Although the wave functions of the top and the bottom slab have a significant spatial overlap, their opposite spin causes the tunneling current to become very low (as shown in the third black dot in Fig. 3), resulting in a very low trough current for the device. Figure 4(d) shows the band structure and the wave functions at a bias $V_{\rm pn}$= 0.18 eV. This corresponds to the final black dot in Fig. 3. We see that the wave functions of the same spin overlap resulting in a finite tunneling current.

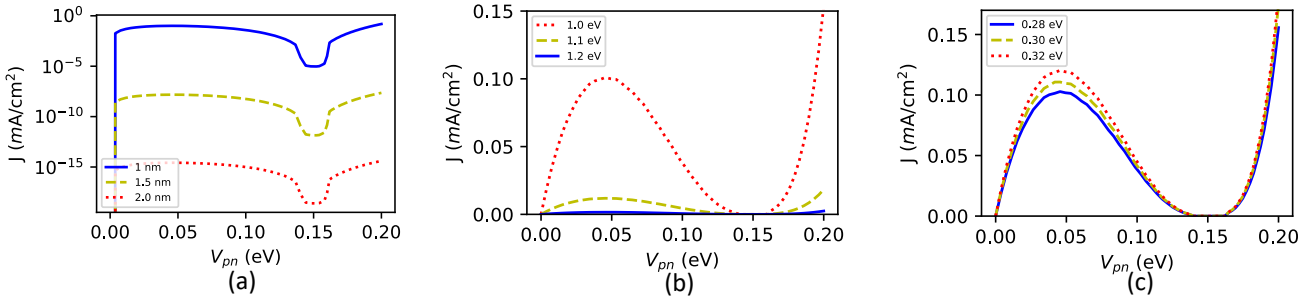

FIG. 5: (a) Current density of our propsed TI NDR device for tunnel barrier thicknesses of t=1.0 nm, 1.5 nm, and 2.0 nm. The magnitude of the current decreases while the shape remains constant as barrier width increases (b) Current density of the NDR device with tunnel barrier heights of V_{onsite}=1.0 eV, 1.1 eV and 1.2 eV. The magnitude of the current decreases while the shape remains constant with increasing barrier height (c) Current density for the NDR device with band gaps E_{g}=0.28 eV, 0.30 eV, and 0.32 eV. Changing the bandgap has little impact on the current density.

To quantify the overlap, we inspect the transition element for different bias conditions. For a bias of 0.05 eV, the transition element $|M|^2 = 2.32\times10^6$ (eV)^2. At the point where V_{pn}=ΔE_{F}=0.15 eV the transition element is significantly lower at $|M|^2 = 1.10$ (eV)^2. At $V_{\text{pn}} = 0.18$ eV, significantly larger than ΔE_{F}, the transition element has once again increased to be on the same order as for 0.05 eV bias at $|M|^2 = 1.76\times10^6$ (eV)^2. The transition element in the case of $V_{\text{pn}} = 0.18$ eV being lesser gives rise to lower current as compared to $V_{\text{pn}} = 0.05$ eV as can be seen in comparing the values of the current at the second and fourth black dots in Fig. 3. Both $V_{\text{pn}} = 0.05$ eV and 0.18 eV have a significantly higher M value than the value at V_{pn}=ΔE_{F}.

III.2. Parametric Device Analysis

When studying the NDR tunneling current, there are several parameters of interest. The first of these parameters is the relative Fermi level of the two slabs. The second parameter is the barrier height and barrier thickness. The final parameter is the bandgap of the slabs, the range of energy between the surface states and the first bulk states.

Figure 5(a) shows the current density as a function of applied bias for tunnel barrier thickness t=1.0 nm, t=1.5 nm, and t=2.0 nm. The shape of the current density remains the same, as does the biases at which the peak and trough currents occur. However, as the thickness of the tunnel barrier between the slabs increases, the magnitude of the current rapidly decreases. This is expected as increasing the gap between the TI slabs decreases the tunneling probability.

Figure 5(b) shows the current density for the tunnel barrier on-site potentials V_{onsite}=1 eV, 1.1 eV, and 1.2 eV. The magnitude of the current density decreases with increasing tunnel barrier on-site potential. The increasing potential increases the tunnel barrier. Since the TIs are unaltered, only the magnitude is affected, not the shape of the J-V curve.

Figure 5(c) shows how the current density changes when the TI bandgap E_{g}= 0.28 eV, 0.30 eV, or 0.32 eV. E_{g} sets the value of M in the TI Hamiltonian. Altering the bandgap means that our $\mathbf{k}\cdot\mathbf{p}$ Hamiltonian either models Bi_2Se_3 under chemical or mechanical strain, or a different hypothetical 3D TI. The small divergence from the results for Bi_2Se_3 show that another 3D TI will yield J-V characteristics similar to the ones we calculated for Bi_2Se_3 and the small dependence of the J-V on TI bandgap. The peak current increases when the bandgap increases from 0.28 eV to 0.32 eV. The relatively small change suggests that changing the TI of both slabs has little impact on the overall current density as long as the Dirac cone is maintained in the bandgap.

IV. CONCLUSION

We have presented a NDR device based on 3D Bi_2Se_3 slabs sandwiching a tunnel barrier material. The presented device utilizes the spin-momentum locking of the surface states of 3D TIs resulting in a spin-dependent tunneling. We used the Bardeen Transfer Hamiltonian method, we calculated the tunneling current between the two slabs. We have shown that the presented NDR device, unlike conventional NDR devices, can have a trough current almost zero resulting in a very high peak to trough ratio. Recent devices, such as van der Waals nanostructures and InAs/Gasb Core-Shell Nanowires [31, 32] show peak to trough ratios of 4 and 8.69 respectively. This is significantly lower the peak to trough ratio of our device. While the ideal system tested here presents a very low trough current, impurities in a real device may cause the current in a real device to be higher. Nevertheless, this device still has lower trough current than other devices. The V_{pn} at which the trough occurs can be tuned by tuning the Fermi level shift between both slabs. We have seen that the peak of these J-V curves occurs at $V_{\text{pn}}\approx \Delta E_{\text{F}}/3$. Moreover, we have

shown that changing the TI material does not have a significant impact on the shape of the J-V curve the device produces. The two-terminal architecture of the presented 3D tunnel diodes makes our proposed device easy to manufacture [26] and conduct experiments on as compared to other novel NDR devices such as graphene nanoribbons and graphene quantum dots. The proposed device can be fabricated using molecular beam epitaxy [33, 34] [35].

V. ACKNOWLEDGEMENTS

This material is based upon work supported by the National Science Foundation under Grant No. 1802166. This work was supported in part by the Semiconductor Research Corporation (SRC) by the NEWLIMITS Center and NIST through award number 70NANB17H041.

VI. APPENDIX

VI.1. Calculating Band Structure and Wave Functions for a TI Slab

To calculate the band structure of a TI slab we start with the $\mathbf{k}\cdot\mathbf{p}$ Hamiltonian from equation (1). To get a slab band structure as opposed to a bulk band structure, we discretize in the out-of-plane direction by replacing k_z with -$i\frac{d}{dz}$, employing the treatment described by Qi et al.[36]. To find the band structures numerically we use finite differences so that $\frac{df}{dz} \approx \frac{f(z+\Delta z)-f(z-\Delta z)}{2\Delta z}$ and $\frac{d^2f}{dz^2} \approx \frac{f(z+\Delta z)-2f(z)+f(z-\Delta z)}{(\Delta z)^2}$ where Δz is the step size. In our case, we took a step size of $\Delta z = 1$ Å. This leads to n_{TI}=100 discrete steps in the TI slab and n_B=110 steps in the tunnel barrier. The systems of the p-doped and n-doped slabs are overlaid, meaning the effective barrier size is equal to the total system size minus 2 times the TI slab size. To solve the Hamiltonian numerically, for both the slab and tunnel barrier Hamiltonians, we take a Kroneker product of the $\mathcal{H}_{\mathrm{TI}}$ and an identity matrix of dimensions of 100×100 for the slab and a Kroneker product of $\mathcal{H}_{\mathrm{D}}$ and identity matrix of dimensions 110×110 for the tunnel barrier. Note that prior to accounting for transitions using the Bardeen Transfer Hamiltonian, when considering the n-slab, the p-slab is modeled using the tunnel barrier Hamiltonian and vice versa.

However, since we are calculating the band structure of the slab with a connected tunnel barrier, we must combine our slab and tunnel barrier Hamiltonians to account for a single system. We define Hamiltonians for each TI slab with a tunnel barrier as shown in Eq. (6) for the p-doped slab and Eq. (7) for the n-doped slab

$$H_{\mathrm{p}} = \begin{pmatrix} H_{\mathrm{D}} & W_{\mathrm{T,D}} \\ W_{\mathrm{B,TI}} & H_{\mathrm{TI}} \end{pmatrix} \tag{6}$$

$$H_{\mathrm{n}} = \begin{pmatrix} H_{\mathrm{TI}} & W_{\mathrm{T,TI}} \\ W_{\mathrm{B,D}} & H_{\mathrm{D}} \end{pmatrix} \tag{7}$$

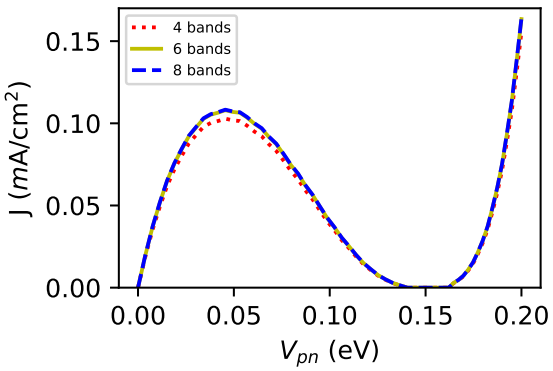

FIG. 6: Current density for a TI slab with increasing number of calculated bands.

Here the numerically evaluated Hamiltonians contain the slab and tunnel barrier Hamiltonians as the diagonal elements and connection terms W as the off-diagonal elements.

The dimensions of the connection terms $4n_{\mathrm{TI}} \times 4n_{\mathrm{D}}$. The connection terms are zero matrices with the exception of 4 elements in the bottom left corner for $W_{\mathrm{T,TI}}$ and $W_{\mathrm{T,D}}$ and the top left corner for $W_{\mathrm{B,TI}}$ and $W_{\mathrm{B,D}}$. The exact form of W_{T} can be seen in Eq. (8) with W_{B} being the adjoint of W_{T}.

$$W_T = \frac{-D_1}{(\Delta z)^2} \begin{bmatrix} 0 & \dots & \dots & \dots & \dots & \dots & 0 \\ \vdots & \vdots & \vdots & \dots & \dots & \dots & \vdots \\ \vdots & \vdots & \vdots & 0 & 0 & \dots & \vdots \\ \vdots & \vdots & 0 & 1 & 0 & \dots & \vdots \\ \vdots & 0 & 1 & 0 & \vdots & \vdots & \vdots \\ 0 & 1 & 0 & \dots & \ddots & \vdots & \vdots \\ 1 & 0 & \dots & \dots & \dots & \dots & 0 \end{bmatrix} \tag{8}$$

$$W_B = W_T^{\dagger} \tag{9}$$

VI.2. Change in Current Density with Increasing Calculated bands

In Fig. 6 we can see the current density plotted for 4 bands, 6 bands, and 8 bands calculated at $\Delta E_{\mathrm{F}} = 0.15$ eV. We see that the magnitude of the current is affected, but there is no impact on the shape. The change in current is relatively small. For a change between four bands and six bands, the maximum divergence is ≈ 5%. The change in current with increasing considered bands decreases as we consider additional bands. For example, the difference in current for a calculation accounting for six versus eight bands is only ≈ 0.3%.

VII. REFERENCES

[1] M. J. Gilbert, Communications Physics **4**, 70 (2021).
[2] W. G. Vandenberghe and M. V. Fischetti, Nature communications **8**, 1 (2017).
[3] S. Tiwari, M. L. V. de Put, B. Sorée, and W. G. Vandenberghe, 2D Materials **6**, 025011 (2019).
[4] A. R. Mellnik, J. S. Lee, A. Richardella, J. L. Grab, P. J. Mintun, M. H. Fischer, A. Vaezi, A. Manchon, E.-A. Kim, N. Samarth, and D. C. Ralph, Nature **511**, 449 (2014).
[5] N. H. D. Khang, Y. Ueda, and P. N. Hai, Nature Materials **17**, 808 (2018).
[6] M. He, H. Sun, and Q. L. He, Frontiers of Physics **14**, 1 (2019).
[7] M. A. Bandres, S. Wittek, G. Harari, M. Parto, J. Ren, M. Segev, D. N. Christodoulides, and M. Khajavikhan, Science **359** (2018).
[8] H. Wu, F. Groß, B. Dai, D. Lujan, S. A. Razavi, P. Zhang, Y. Liu, K. Sobotkiewich, J. Förster, M. Weigand, G. Schütz, X. Li, J. Gräfe, and K. L. Wang, Advanced Materials **32**, 2003380 (2020).
[9] Z. Wu, G. Liang, W. K. Pang, T. Zhou, Z. Cheng, W. Zhang, Y. Liu, B. Johannessen, and Z. Guo, Advanced Materials **32**, 1905632 (2020).
[10] Z. Yang, E. Lustig, G. Harari, Y. Plotnik, Y. Lumer, M. A. Bandres, and M. Segev, Phys. Rev. X **10**, 011059 (2020).
[11] D. Flötotto, Y. Ota, Y. Bai, C. Zhang, K. Okazaki, A. Tsuzuki, T. Hashimoto, J. N. Eckstein, S. Shin, and T.-C. Chiang, Science advances **4**, eaar7214 (2018).
[12] W. Tang, A. Politano, C. Guo, W. Guo, C. Liu, L. Wang, X. Chen, and W. Lu, Advanced Functional Materials **28**, 1870219 (2018).
[13] P. Sharma, M. Kumar, and V. Awana, Applied Physics A **127**, 1 (2021).
[14] C.-X. Zhao and J.-F. Jia, Frontiers of Physics **15**, 1 (2020).
[15] G. Gaddemane, W. G. Vandenberghe, M. L. Van de Put, S. Chen, S. Tiwari, E. Chen, and M. V. Fischetti, Phys. Rev. B **98**, 115416 (2018).
[16] X. Wang, C. Xu, H. Hu, P. Wang, G. Bian, W. Tan, S. Brown, and T.-C. Chiang, EPL (Europhysics Letters) **119**, 27002 (2017).
[17] H. Wang, J. Kally, J. S. Lee, T. Liu, H. Chang, D. R. Hickey, K. A. Mkhoyan, M. Wu, A. Richardella, and N. Samarth, Physical review letters **117**, 076601 (2016).
[18] W. G. Vandenberghe, C. L. Hinkle, and M. V. Fischetti, "Memory devices based on gate controlled ferromagnestism and spin-polarized current injection," (2016), uS Patent 9741416B1.
[19] Y. Wu, D. B. Farmer, W. Zhu, S.-J. Han, C. D. Dimitrakopoulos, A. A. Bol, P. Avouris, and Y.-M. Lin, ACS nano **6**, 2610 (2012).
[20] R. Van Zyl, W. Perold, and R. Botha, in *Proceedings of the 1998 South African Symposium on Communications and Signal Processing-COMSIG'98 (Cat. No. 98EX214)* (IEEE, 1998) pp. 407–412.
[21] J. Chen, M. A. Reed, A. M. Rawlett, and J. M. Tour, Science **286**, 1550 (1999).
[22] H. Ren, Q.-X. Li, Y. Luo, and J. Yang, Applied Physics Letters **94**, 173110 (2009), https://doi.org/10.1063/1.3126451.
[23] J. M. Marmolejo-Tejada and J. Velasco-Medina, Microelectronics Journal **48**, 18 (2016).
[24] P. Sharma, L. S. Bernard, A. Bazigos, A. Magrez, and A. M. Ionescu, ACS nano **9**, 620 (2015).
[25] S. Sharma, C.-A. Cheng, S. R. M. Santiago, D. N. Feria, C.-T. Yuan, S.-H. Chang, T.-Y. Lin, and J.-L. Shen, Physical Chemistry Chemical Physics (2021).
[26] A. T. Barton, L. A. Walsh, C. M. Smyth, X. Qin, R. Addou, C. Cormier, P. K. Hurley, R. M. Wallace, and C. L. Hinkle, ACS applied materials & interfaces **11**, 32144 (2019).
[27] L. A. Walsh, A. J. Green, R. Addou, W. Nolting, C. R. Cormier, A. T. Barton, T. R. Mowll, R. Yue, N. Lu, J. Kim, *et al.*, ACS nano **12**, 6310 (2018).
[28] H. Zhang, C.-X. Liu, X.-L. Qi, X. Dai, Z. Fang, and S.-C. Zhang, Nature physics **5**, 438 (2009).
[29] J. Bardeen, Phys. Rev. Lett. **6**, 57 (1961).
[30] M. L. Van de Put, W. G. Vandenberghe, B. Sorée, W. Magnus, and M. V. Fischetti, Journal of Applied Physics **119**, 214306 (2016).
[31] S. Fan, Q. A. Vu, S. Lee, T. L. Phan, G. Han, Y.-M. Kim, W. J. Yu, and Y. H. Lee, ACS nano **13**, 8193 (2019).
[32] C.-W. Hsu, Q. H. Luc, P. Huang, J. Y. Wu, N. A. Tran, E. Y. Chang, *et al.*, in *ECS Meeting Abstracts*, 51 (IOP Publishing, 2020) p. 3835.
[33] M. A. Herman and H. Sitter, *Molecular beam epitaxy: fundamentals and current status*, Vol. 7 (Springer Science & Business Media, 2012).
[34] L. A. Walsh and C. L. Hinkle, Applied Materials Today **9**, 504 (2017).
[35] Y. R. Sapkota, *Physical Properties of Topological Insulator: Bismuth Selenide Thin Films* (Southern Illinois University at Carbondale, 2017).
[36] X.-L. Qi and S.-C. Zhang, Reviews of Modern Physics **83**, 1057 (2011).